Solar-Terrestrial Physics. 2023. Vol. 9. Iss. 1. P. 9–20. DOI: 10.12737/stp-91202302. © 2023
M.B. Krainev, M.S. Kalinin, G.A. Bazilevskaya, A.K. Svirzhevskaya, N.S. Svirzhevsky, Xi Luo, O.P.M. Aslam, Fang Shen, M.D. Ngobeni, M.S. Potgieter. Published by INFRA-M Academic Publishing House

UDC 524.1
DOI: 10.12737/stp-91202302

Received November 30, 2022
Accepted December 28, 2022

MANIFESTATION OF SOLAR WIND COROTATING INTERACTION REGIONS IN GCR INTENSITY VARIATIONS

M.B. Krainev
P.N. Lebedev Physical Institute, RAS, Moscow, Russia, mkrainev46@mail.ru
Shandong Institute of Advanced Technology, Jinan, Shandong, China

M.S. Kalinin
P.N. Lebedev Physical Institute, RAS, Moscow, Russia, kalininms@lebedev.ru

G.A. Bazilevskaya
P.N. Lebedev Physical Institute, RAS, Moscow, Russia, bazilevskayaga@lebedev.ru

A.K. Svirzhevskaya
P.N. Lebedev Physical Institute, RAS, Moscow, Russia, svirzhevskayaak@lebedev.ru

N.S. Svirzhevsky
P.N. Lebedev Physical Institute, RAS, Moscow, Russia, svirzhevskyns@lebedev.ru

Xi Luo
Shandong Institute of Advanced Technology, Jinan, Shandong, China, xi.luo@iat.cn

O.P.M. Aslam
Shandong Institute of Advanced Technology, Jinan, Shandong, China, Aslamkir2003@gmail.com

Fang Shen
National Space Science Center, Beijing, China, fshen@spaceweather.ac.cn

M.D. Ngobeni
North-West University, Centre for Space Research, Potchefstroom, South Africa, Donald.ngobeni@nwu.ac.za
School of Physical and Chemical Sciences, North-West University, Mmabatho, South Africa

M.S. Potgieter
Shandong Institute of Advanced Technology, Jinan, Shandong, China,
Institute for Experimental and Applied Physics, Christian Albrechts University, Kiel, Germany, potgieter@physik.uni-kiel.de

Abstract. The regions of interaction between solar wind streams of different speed, known as corotating interaction regions, form an almost constantly existing structure of the inner heliosphere. Using observational data on the main characteristics of the heliosphere, important for GCR modulation, and the results of 3D MHD modeling of corotating interaction regions, and Monte Carlo simulation of recurrent GCR variations, we analyze the importance of the corotating interaction regions for longitude-averaged characteristics of the heliosphere and GCR propagation, and possible ways for simulating long-term GCR intensity variations with respect to the corotating interaction regions.

Keywords: heliosphere, corotating interaction regions, galactic cosmic rays, GCR modulation, long-term GCR variations, 27-day GCR intensity variation, MHD approximation, Monte Carlo method.

INTRODUCTION

Solar wind (SW) corotating interaction regions (CIRs) are regions of the inner heliosphere at low and middle latitudes, which result from the interaction between SW streams of different speed with spatial redistribution of matter and heliospheric magnetic field (HMF) [Belcher, Davis, 1971; Simpson, 1998; Richardson, 2018]. CIRs rotate with the Sun and near Earth manifest themselves as so-called recurrent variations in heliospheric characteristics and galactic cosmic ray (GCR) intensity with periods close to the period of solar rotation ($T_\odot \approx 27$ days). Since the mid-1970s, when the concept of global heliospheric current sheet (HCS), curved due to the longitude asymmetry of coronal holes, was formulated, the formation of CIRs has been associated with an increase in the SW velocity with distance from HCS [Schulz, 1973; Hundhausen, 1972; Wang, Sheeley, 1990]. A lot of works have been devoted to the formation and analysis of recurrent variations, for example, [Pizzo, Gosling, 1994; Gosling, Pizzo, 1999; Kóta, Jokipii, 1991, 1998; Modzelewska, Alania, 2012; Modzelewska et al., 2020]. Modern models of CIR calculation are overviewed and analyzed, for example, in [Riley et al., 2012], and the problems of simulating interplanetary mass ejections, which largely overlap those of simulating CIRs, are addressed in [Mays et al., 2015]. We are particularly interested in recent comprehensive numerical studies on the heliosphere and GCRs during specific solar rotation periods [Wiengarten et al., 2014; Kopp et al., 2017; Guo, Florinski, 2014, 2016; Shen at al., 2018; Luo et al., 2020].

By a comprehensive study is meant:

1) detailed numerical analysis of characteristics in a layer between the photosphere ($r=r_\odot$), where the magnetic field distribution is known from observations, and possibly some other characteristics, and the base of the heliosphere ($r=r_{in}=0.1\div0.2$ AU$\approx(20\div40)r_\odot$) to determine the internal boundary conditions in the heliosphere (see [Odstrcil, 2003]);

2) numerical calculation of the characteristics (SW velocity **V**, density ρ, temperature *T*, HMF, and their associated pressure *P*) in the magnetohydrodynamic (MHD) approximation to an outer boundary r_{out}^{MHD} [Wiengarten et al., 2014; Shen at al., 2018];

3) further development of the heliosphere model from r_{out}^{MHD} to its outer boundary $r_{out}\approx 120$ AU from some simple models (for example, the constant SW velocity as a function of *r* and the Parker HMF model) and calculation of the GCR intensity in the composite model of the heliosphere $r_{in}\le r\le r_{out}$. The heliospheric characteristics and the GCR intensity were calculated in 3D geometry (r, θ, φ in the heliocentric equatorial spherical coordinate system), with the characteristics determined by finite difference methods, and the GCR intensity in [Kopp et al., 2017; Guo, Florinski, 2014, 2016; Luo et al. al., 2020] was calculated by the Monte Carlo (MC) method.

Comprehensive studies on the heliosphere and GCRs with the full-blown first stage (determination of internal boundary conditions) based on scanning of solar magnetic fields on the solar photosphere and numerical reconstruction of the distribution of desired characteristics (first of all, the SW velocity and the magnetic field) at the base of the heliosphere [Wiengarten et al., 2014; Shen at al., 2018] are hereinafter called real. In addition to the real studies, of particular interest are those dealing with internal boundary conditions [Guo, Florinski, 2014, 2016]: a simple shape of HCS — usually a great circle tilted to the equator at an angle α_t (the model of tilted HCS [Kóta, Jokipii, 1983]), and a dependence of the SW velocity on the angular distance from HCS are specified. Such studies with a small number of parameters that allow us to discern the basic laws of the formation and evolution of CIRs and GCR intensity in the heliosphere are further referred to as simplified. Note that such a simplified approach to specifying heliospheric characteristics, such as the HCS shape, is often used to study GCR variations, as pioneered by [Kóta, Jokipii, 1983].

As mentioned above, the main task of the final stage of these comprehensive works was to study recurrent GCR intensity variations arising from the longitudinal asymmetry in solar and heliospheric factors. Nonetheless, in addition to the significant longitudinal inhomogeneity, CIRs can also greatly affect longitude-averaged characteristics of the heliosphere and hence long-term GCR intensity variations (with a characteristic time $\tau\ge T_\odot$). Our paper tests the assumption about CIR effect on the mean characteristics of the heliosphere and analyzes how to take this effect into account when describing the long-term GCR intensity variations.

Section 1 illustrates the basic concepts of CIR formation and 27-day variations in heliospheric characteristics and GCR intensity. Section 2 examines the behavior of longitude-averaged heliospheric characteristics, which we consider as indirect evidence of the CIR effect on them. Section 3 explores the direct impact of SW streams of different speed with formation of CIRs and recurrent variations in heliospheric characteristics, using MHD simulation data. Section 4 discusses 3D and 2D transport equations describing CR propagation in the heliosphere, relationships between them, and methods of calculating recurrent and long-term GCR intensity variations. The main heliospheric factors important for the formation of these variations are isolated. Section 5 analyzes ways to simulate long-term GCR intensity variations with respect to CIRs. Section 6 contains discussion and conclusions.

1. CIR FORMATION AND 27-DAY VARIATIONS IN HELIOSPHERIC CHARACTERISTICS AND GCRs

The simplest and most widespread Parker HMF model [Parker, 1958a]:

$$B_r(r,\theta,\varphi)=\frac{B_0(\theta,\varphi)r_{in}^2}{r^2}, \tag{1a}$$

$$B_\theta(r,\theta,\varphi)=0, \tag{1b}$$

$$B_\varphi(r,\theta,\varphi)=-\frac{\omega(r-r_{in})\sin\theta}{V_r}B_r(r,\theta,\varphi), \tag{1c}$$

where B_0 is the radial HMF component at a distance r_{in}; ω is the angular velocity of solar rotation, suggests a purely kinematic formation of HMF without any interaction between adjacent SW streams.

If the SW velocity at the base of the heliosphere did not depend on longitude φ, as is assumed when constructing three HMF lines, shown in blue in Figure 1 (for V_r=300 km/s), no corotating interaction regions would arise. However, if at the base of one of these field lines (φ=60°) the SW velocity is minimal such that at longitudes close to it (more easterly φ=50° and more westerly φ=70°) V_r=320 km/s, the corresponding Parker HMF lines are less twisted in a spiral (rubricated in Figure 1). With distance from the Sun, the western red field line is seen to increasingly diverge from the blue one, which indicates a region of HMF weakening. The eastern red field line becomes closer to the original one, which implies that the medium compresses and HMF strengthens, and at a distance $r\approx 2.5$ AU the red and blue HMF lines intersect. This means that already at distances much shorter than 2.5 AU the kinematic model stops working and HMF should be simulated in the MHD approximation. The calculations in the MHD approximation for SW and HMF characteristics demonstrate that CIRs are formed with an interface and standing shock waves; they have been described in many works (e.g., [Pizzo, Gosling, 1994]).

Note that the presence of the longitude SW velocity gradient at the base of the heliosphere leads to the formation of not only regions of enhanced HMF with all their features, which are often called corotating interaction regions, but also regions of rarefied plasma and weakened HMF. As shown below, these two groups of regions with distance from the Sun evolve in a certain way and both are very important for GCR propagation.

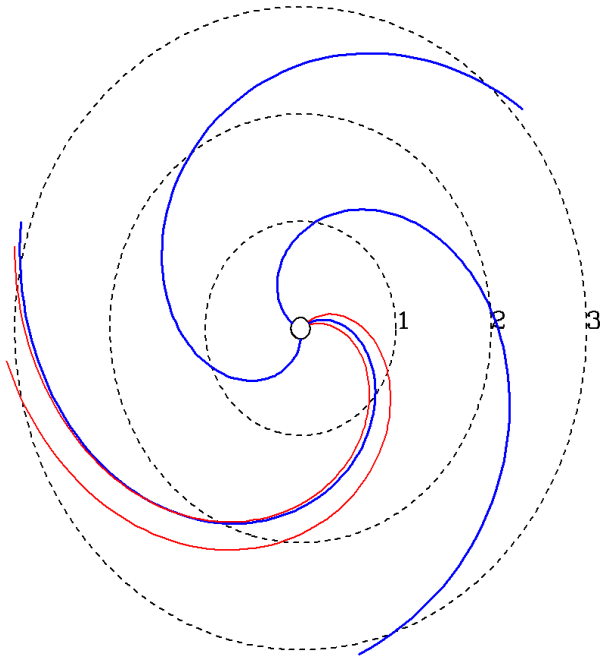

Figure 1. Configuration of Parker HMF lines, which gives rise to corotating interaction regions of SW streams of different speed. Blue curves are three HMF lines corresponding to Parker model (1) and coming from the inner boundary of the heliosphere (r=r_{in}=0.1 AU, solid circle) from different helioequator longitudes at the same SW speed (V_r=300 km/s). Red curves are field lines according to the Parker model, originating at a higher SW speed (V_r=320 km/s) from the vicinity of one of the blue lines. Dashed circles and numbers near them indicate the radial distance in AU

Therefore, not to introduce additional terms, we will refer to the combination of regions of both HMF strengthening and weakening as corotating interaction regions of SW streams of different speed.

As already noted in Introduction, the minimum speed values at the base of the corona are observed in global HCS. The shape of HCS is estimated based on the results of daily scanning of the Sun's magnetic field [http://wso.stanford.edu] and usually features the so-called quasi-tilt α_{qt}, equal to half of the range of latitudes the HCS occupies, and a magnetic equator latitude λ_{me} — the middle of this latitude range. Note that this range of heliolatitudes is often called the zone of the HMF sector structure since there are several longitude sectors of different HMF polarity (antisunward/sunward).

When observed from Earth orbit, the SW and HMF characteristics, including density ρ, temperature T, and total pressure P, as well as their driven GCR intensity J, exhibit, along with sporadic and long-term variations, recurrent or 27-day variations. Note, however, that, strictly speaking, the use of this term is valid only if the distribution of these characteristics is stationary at the base of the heliosphere in a coordinate system rotating with the Sun. In the following sections, we discuss the results of simulation of CIRs and recurrent variations. Therefore, in Figure 2 displaying sporadic, 27-day, and long-term GCR intensity variations, as well as the quasi-tilt α_{qt} for 2004–2009 and 2015–2020, brackets on panels *a* and *b* indicate when the stationary approximation is, at least approximately, valid, anyway for the GCR intensity and the degree of HCS waviness as the most important for the formation of the CIR structure. It can be seen that in the first approximation the quasistationarity of the situation is fulfilled in 2007.5–2008.5 and in 2018. In 2016, as well as in 2014–2015 [Krainev et al., 2017], when the amplitude of the 27-day variation in the high-energy GCR intensity is significantly higher, as inferred from the behavior of the averaged characteristics, the situation at the base of the heliosphere is far from stationary.

Notice that both strictly recurrent and long-term GCR intensity variations during low sunspot activity are quasistationary, determined by a slow change in the characteristics of the Sun.

2. INDIRECT EVIDENCE OF CIR EFFECTS ON MEAN HELIOSPHERE CHARACTERISTICS

Some conclusions about the CIR effect not only on the longitude asymmetry, but also on the longitude-averaged HMF characteristics can be drawn from data from the spacecraft (SC) scanning significant heliosphere regions, and by comparing the results with those expected by the Parker HMF model, which, in our opinion, is valid in the absence of CIRs.

As can be seen from the Voyager 1 and 2 trajectories shown in Figure 3, *a*, both spacecraft are almost constantly in the zone of the HMF sector structure, where SW streams of different speed generally interact with each other, at least in the inner heliosphere. Figure 3, *b*, *c* shows respectively radial dependences of the regular HMF radial component modulus $|B_r|$ according to Voyager 1 and 2 data, as well as approximation of their power-law dependence on radial distance, $|B_r| \sim r^{-\gamma}$. For both spacecraft, the power-law dependence γ in the entire range of distances (γ_{V1}=1.196 ±0.005; γ_{V2}=0.922 ±0.006) and in the inner heliosphere (γ_{V1}=1.41 ±0.02; γ_{V2}=1.29 ±0.02) is much lower than γ=2 corresponding to Parker model (1a). Note that the approximation $|B_r| \sim r^{-\gamma}$ to r=10 AU is considered separately because at these distances the accuracy of measurement of B_r is quite high [Burlaga et al., 2002]. The difference between the observed HMF and the Parker model in the inner heliosphere has also been reported in other works [Khabarova, Obridko, 2012; Svirzhevsky et al., 2021]. This is consistent with our assumption about the CIR effect on the large-scale heliosphere characteristics since one of the results of the interaction between SW streams of different speed should be the transfer of energy from a more energetic solar wind to HMF and a slower decrease in the latter with distance.

However, probably the best way to demonstrate the CIR effect on the deviation of observed HMF from the Parker one is to compare measurements along the trajectory of the Ulysses spacecraft inside and outside the zone of the HMF sector structure [Smith, 2011].

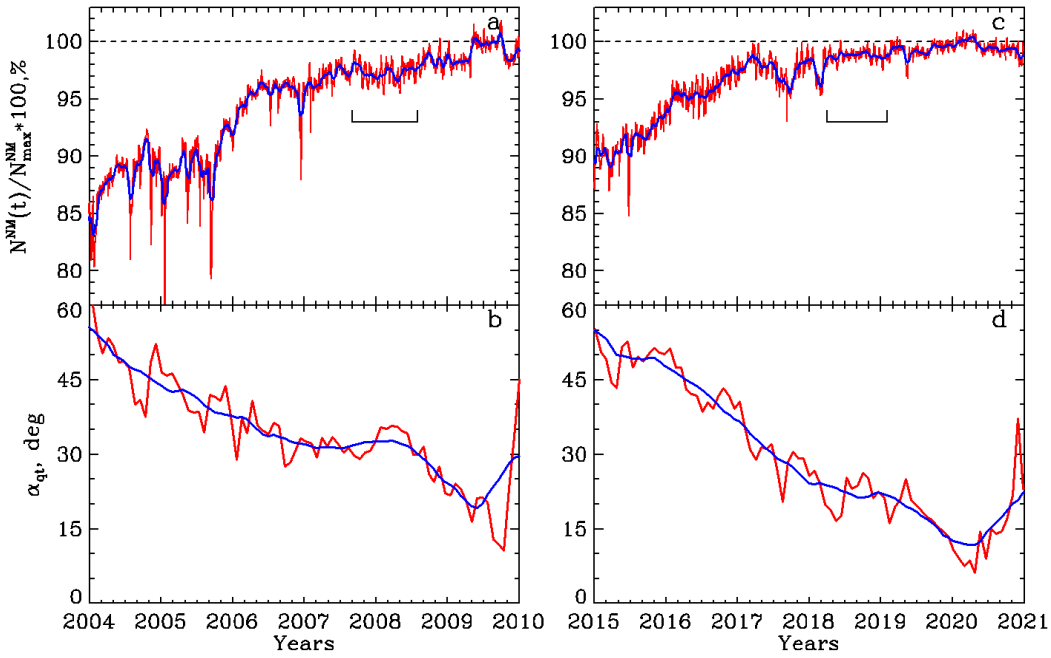

Figure 2. Variations in the GCR intensity and the degree of HCS waviness during periods of sunspot growth and minimum: daily average count rate of the neutron monitor Moscow (red curves) and that smoothed with a period of 27 days (blue curves) normalized to 100 % during maximum intensity in 2004–2009 and 2015–2020 respectively [http://cr0.izmiran.ru/mosc/main.htm] (*a*, *c*); *b*, *d* are α_{qt} values [http://wso.stanford.edu, a variant of the classic model] for each Carrington rotation (red curves) and their values smoothed with a period of 1 year (blue curves) for the two periods. Brackets on panels *a* and *c* indicate quasistationarity periods

As Figure 4 suggests, in the region encompassed by latitudinal boundaries of this zone, due to the rapid variability of the SW velocity in longitude, the mean SW velocity and the HMF components vary greatly with time. In this case, observed B_φ is in poor agreement with the value of this component in the Parker model by (1), calculated from the observed values of B_r and V_r. As soon as SC leaves the zone of the HMF sector structure, the SW velocity increases rapidly, the radial HMF component, normalized to the field value at r=1 AU, takes the sign of high-latitude solar fields in the corresponding hemisphere, its value weakly depends on latitude, and the correspondence between observed B_φ and this component, calculated from the observed values of B_r and V_r by Parker model (1), significantly improves.

Two bottom panels in Figure 4 show the time variation in characteristics of the frequency spectrum of HMF inhomogeneities $P(f) = P_0 f^{-\gamma_{HMF}}$, which is averaged for each solar rotation. Both the spectrum power P_0 at a fixed frequency and the spectral index γ_{HMF} are significantly different in the zone of the sector structure and outside it, and may depend on heliocentric distance.

3. DESCRIPTION OF RECURRENT VARIATIONS IN CIR DRIVEN HELIOSPHERIC CHARACTERISTICS

As mentioned above, for the validity of the Parker HMF model, which suggests a purely kinematic formation of HMF by the solar wind, a uniform SW velocity as a function of longitude is required. If this condition is violated, which is common practice in the vicinity of curved HCS at the base of the heliosphere, the reverse effect of magnetic and thermal pressures on the velocity field becomes noticeable and a system of MHD equations has to be solved to define the heliospheric characteristics. In [Wiengarten et al., 2014; Shen at al., 2018; Luo et al., 2020], to determine the field distribution of the SW velocity **V** and HMF **B**, the authors searched for a steady-state solution of the nonstationary system of equations with constant boundary conditions. System (2), in addition to the equations for **V** and **B**, includes

$$\frac{\partial \rho}{\partial t} + \nabla \cdot \rho \mathbf{V} = 0, \tag{2a}$$

$$\frac{\partial \rho \mathbf{V}}{\partial t} + \nabla \left[\left(P + \frac{B^2}{2\mu_0} \right) \mathbf{I} + \rho \mathbf{V}\mathbf{V} - \frac{\mathbf{B}\mathbf{B}}{\mu_0} \right] = -\frac{\rho G M_S}{r^2} \frac{\mathbf{r}}{r} + \mathbf{V} \cdot \mathbf{f}, \tag{2b}$$

$$\frac{\partial \mathbf{B}}{\partial t} + \nabla \cdot \left[\mathbf{V}\mathbf{B} - \mathbf{B}\mathbf{V} \right] = 0, \tag{2c}$$

$$\frac{\partial P}{\partial t} + \nabla \cdot \rho \mathbf{V} = -(\gamma - 1) P \nabla \cdot \mathbf{V}, \tag{2d}$$

for the SW density ρ and pressure P, as well as the gravity constant G, the solar mass M_S, and the polytropic index γ of the equation of state. System of equations (2) was solved in a spherical coordinate system

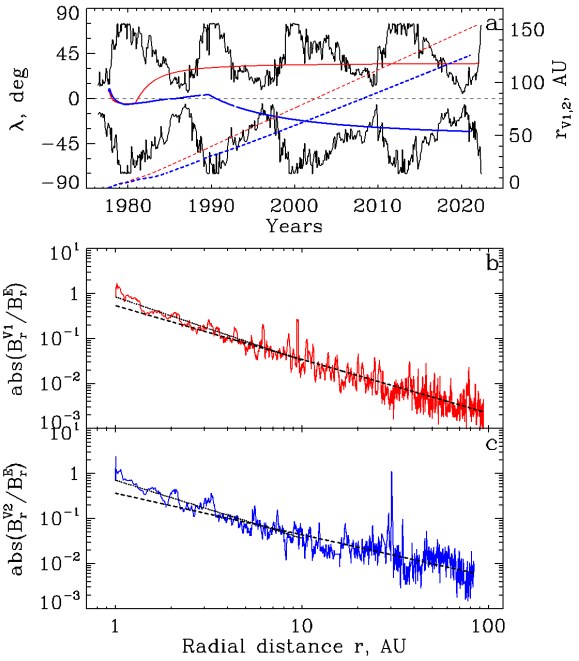

Figure 3. Large-scale heliosphere characteristics as observed by Voyager 1 and 2 [http://omniweb.gsfc.nasa.gov]: trajectories (solar latitude (solid lines), radial distance (dashed lines)) of Voyager 1 (red lines) and Voyager 2 (blue lines) in 1977–2022 (*a*). Black lines are the northern and southern boundaries of the zone of the HMF sector structure; the absolute radial HMF component, smoothed with a period of 27 days, as a function of radial distance for Voyager 1 (red lines) and 2 (blue lines) respectively (*b*, *c*). Dashed black lines indicate approximation of radial dependences by a power-law function for the entire range of distances to a shock wave; dotted lines, to r=10 AU

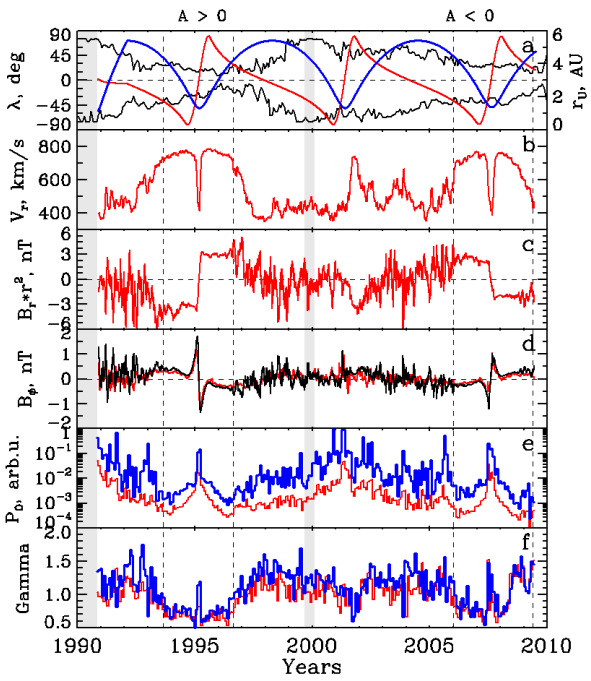

Figure 4. Regular HMF and its fluctuations along the Ulysses trajectory [http://omniweb.gsfc.nasa.gov]: Ulysses trajectories (the red curve is a heliolatitude, the blue curve is a radial distance), as well as the northern and southern boundaries of the HMF sector structure zone (black curves) in 1990–2009 (*a*); SW velocity (*b*); regular HMF's radial and longitude components, smoothed with a period of 27 days, along the Ulysses trajectory (*c*, *d*). The black curve (*d*) is the longitude HMF component according to Parker model (1b) with SW velocity and radial HMF component shown in panels *b*, *c*. Panels *e*, *f* are characteristics (power P_0 and spectral index γ_{HMF}) of the spectrum of HMF inhomogeneities along the Ulysses trajectory. Blue curves are characteristics of the spectrum of HMF inhomogeneities parallel to the mean HMF vector; thinner red curves are those perpendicular to it

rotating with the Sun, so the force **f** contains a noninertial component [Luo et al., 2020]. Below, to demonstrate the importance of the CIR effect on **V** and **B**, we present the results of calculation of these characteristics for Carrington rotation (CR) 2066 of the Sun, January–February 2008 [Luo et al., 2020], when recurrent variations in these characteristics and GCR intensity were fairly significant, and the situation on the Sun was quasistationary (see Figure 2 and its discussion). Note that in this paper we use the MHD simulation results only for the SW velocity and HMF vectors on a rather rare sample from the original mesh in which the simulation was carried out.

Figure 5 compares the distribution of the radial SW velocity and HMF components at the initial level r_{in}=0.19 AU and at the level $r_{out}^{MHD} = 28.44$ AU, to which the calculations were made. It can be seen that at the initial distribution level (Figure 5, *a*, *b*), both V_r and B_r are located relative to HCS with α_{qt}=28.1° and λ_{me}=–8.5°. The SW velocity in HCS is low (V_r=302±6 km/s, where the second value is the root-mean-square width of the distribution) and increases rapidly with distance from it. The longitude derivative $|\partial V_r / \partial\varphi|$, which can be found from the longitude distance between isolines, is the most important parameter for the formation of CIRs. Let us point to its high values near the sections of HCS with a rapid change in its latitude. Finally, note the approximate constancy of $|B_r|$ on the sphere of the initial level: $|B_r|$=80±8 nT. In comparison with the initial level at the outer boundary of the domain of calculation in the MHD approximation (see Figure 5, *c*, *d*), the longitude distribution of V_r becomes more homogeneous. HCS varies greatly both in the degree of waviness (α_{qt}=4.4°) and in the mean position (λ_{me}=10.7°). The distribution of B_r over the outer sphere is very inhomogeneous ($|B_r|$=0.003 ±0.002 nT).

In order to emphasize more strongly that just the SW velocity dependence on longitude affects the HMF distribution, we form a relative difference between the strength calculated in the MHD approximation B^{MHD} and the longitude-averaged strength of Parker $\bar{B}^{Par}(r,\theta)$, calculated by Equations (1), in which B_0 corresponds to the distribution of B_r at the initial level r_{in}, and the SW velocity is equal to longitude-averaged V_r at the initial level:

$$\Delta_{Par}^{MHD}(r,\theta,\varphi) = \frac{\left(B^{MHD}(r,\theta,\varphi) - \bar{B}^{Par}(r,\theta)\right)}{\bar{B}^{Par}(r,\theta)} \cdot 100\ \%. \quad (3)$$

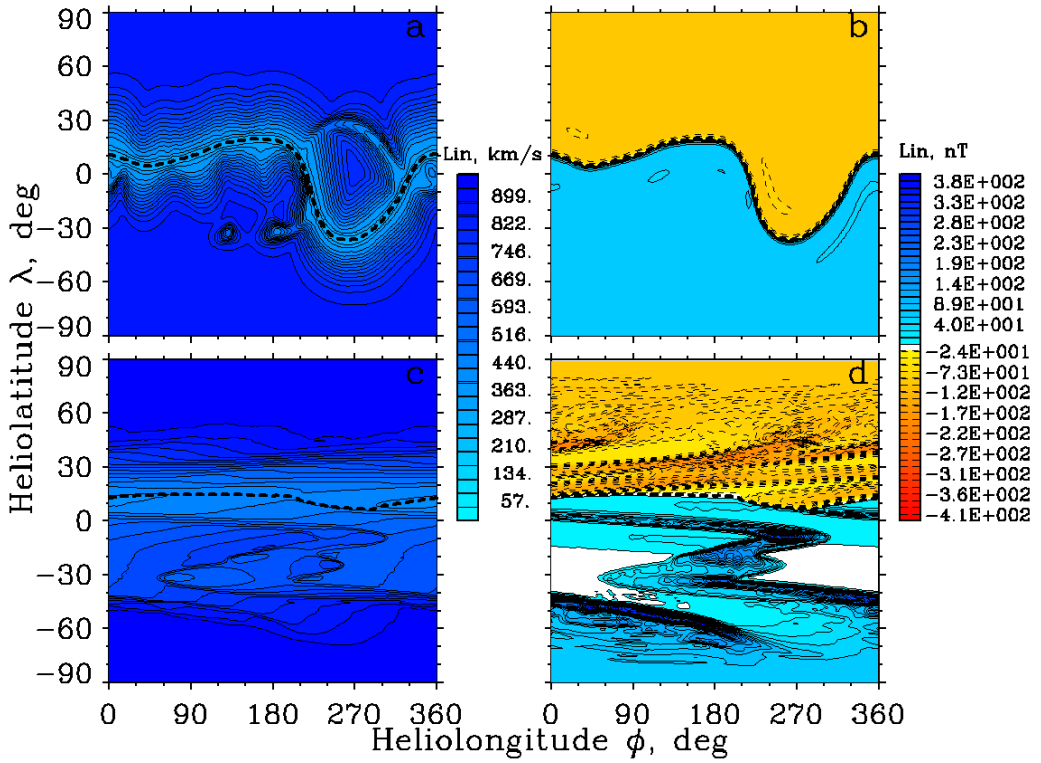

Figure 5. Longitude and latitude distribution of radial components of SW velocity (*a*, *c*) and regular HMF (*b*, *d*) at the initial (r=0.19 AU; panels *a*, *b*) and final (r=28.44 AU; panels *c*, *d*) levels of MHD calculations [Luo et al., 2020]. Distribution of HMF at the final level is normalized to the distribution at the initial level by multiplying B_r by $\left(r_{\text{out}}^{\text{MHD}} / r_{\text{in}}\right)^2$. Black dashed lines mark the HMF position

The top panel in Figure 6 shows the distribution of $\Delta_{\text{Par}}^{\text{MHD}}(\lambda, \varphi)$ over the sphere r=0.94 AU, closest to Earth. The regions where the HMF strength significantly (in some regions, more than hundreds of times) exceeds the Parker one $\bar{B}^{\text{Par}}$, are seen to locate to the left (to the east) of HCS in those its parts where there is a strong decrease in speed as HCS is approached; and to the right (to the west) of HCS are regions of relative weakening of HMF. On the following two panels, the heliolatitude dependence of the SW velocity and HMF strength calculated in the MHD approximation and determined along the projection of the Earth trajectory on the sphere r=0.94 AU is compared with daily average values of these characteristics, using near-Earth observations. There is a significant variation in both calculated characteristics. At the same time, the HMF strength is described by the calculations quite well (except for the peak at φ=150°–180°), whereas the SW velocity variation is in much poor agreement with the calculated one.

The discrepancy between the observations and the calculation results might to some extent be due to different radial distances (for observations r=1 AU, for calculations r=0.94 AU).

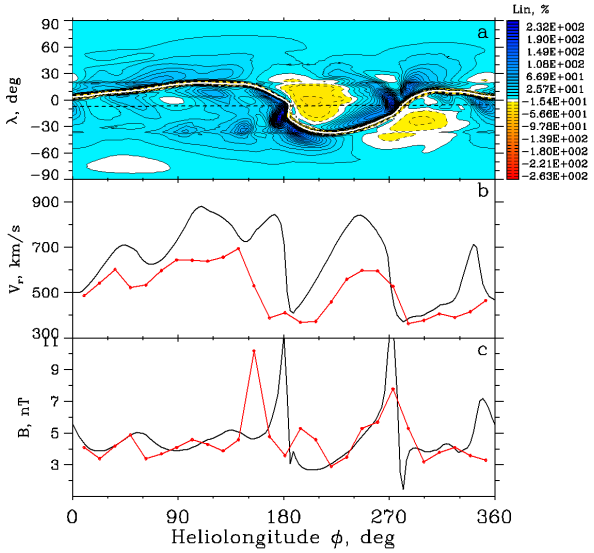

Figure 6. Results of MHD calculation of heliospheric characteristics at r=0.94 AU along the Earth orbit [Luo et al., 2020]: *a* is longitude and latitude distribution of relative difference $\Delta_{\text{Par}}^{\text{MHD}}$ (3) between the HMF strength, calculated in the MHD approximation, and the Parker HMF strength without CIRs. The HCS position is marked with the white dashed line. The black dashed curve indicates Earth's trajectory; *b*, *c* are the radial SW velocity component and the HMF strength respectively. Black lines are the values calculated by Luo et al. [2020]; red broken lines, the daily average values measured at the Earth orbit [http://omniweb.gsfc.nasa.gov]

4. DESCRIPTION OF GCR INTENSITY VARIATIONS

If, as in the study of recurrent variations, we are interested in the GCR intensity distribution

$J(\mathbf{r}, T, t) = p^2 \mathcal{U}(\mathbf{r}, p, t)$ in the heliosphere as a function of all three spatial coordinates (r, θ, φ), it is described by a 3D equation [Parker, 1958b, 1965; Krymsky, 1964; Jokipii et al., 1977] in the stationary case in a coordinate system rotating with the Sun

$$\nabla \cdot (\mathcal{K}_S \nabla \mathcal{U}) - (\mathbf{V} + \mathbf{V}_D) \cdot \nabla \mathcal{U} + \frac{\nabla \cdot \mathbf{V}}{3} \frac{\partial \mathcal{U}}{\partial \ln p} = 0 \qquad (4)$$

for the distribution function $\mathcal{U}(\mathbf{r}, p)$ of particles with momentum p and kinetic energy T at the point (r, θ, φ). The tensor $\mathcal{K}_S$ describes the particle diffusion, $\mathbf{V}$ and $\mathbf{V}_D$ are SW and particle drift velocities in inhomogeneous HMF. If, as in the study of long-term variations, we are interested in the distribution of the longitude-averaged intensity $J(r, \theta, T) = \langle J(r, \theta, \varphi, T) \rangle_\varphi$, by presenting the unknown function and coefficients of Equation (4) as the sum of an axisymmetric part and a three-dimensional additive:

$\mathcal{U} = U + u$, $\mathcal{K}_S = \mathbf{K} + \mathbf{k}$, $\mathbf{V} = \mathbf{V} + \mathbf{v}$, $\mathbf{V}_D = \mathbf{V}_d + \mathbf{v}_d$, we can obtain a 2D equation for $U(r, \theta, p)$:

$$\nabla \cdot (\mathbf{K} \cdot \nabla U) - (\mathbf{V} + \mathbf{V}_d) \cdot \nabla U + \\ + \frac{\nabla \cdot \mathbf{V}}{3} \frac{\partial U}{\partial \ln p} + Q = 0 \qquad (5)$$

with a source term

$$Q = \left\langle \nabla \cdot (k \nabla u) - \mathbf{v} \cdot \nabla u - \mathbf{v}_d \cdot \nabla u + \right. \\ \left. + \frac{\nabla \cdot \mathbf{v}}{3} \frac{\partial u}{\partial \ln p} \right\rangle_\varphi . \qquad (6)$$

By adding the corresponding boundary conditions to transport equations (4) and (5), we obtain differential boundary value problems.

To calculate GCR recurrent variations, knowing variations in heliospheric characteristics, we have to solve Equation (4). In this case, the boundary value problem with differential transport equation (4) can be solved numerically either via a finite difference method, by replacing differential operators with difference operators and using, for example, a fractional step method [Yanenko, 1967], or via a Monte Carlo method, by moving from partial differential transport equations to systems of stochastic differential equations for each pseudo-particle coordinate [Zhang, 1999a, b]. Each of these ways of numerical solution of the boundary value problem with transport equation (4) has its advantages and disadvantages. The Monte Carlo method can much easier find the GCR intensity for the problems with rapidly changing transport equation coefficients in space, as well as for nonstationary problems. Nonetheless, in one run (with a lot of pseudoparticles emitted), the intensity characteristics only for particles of the same energy at one point of the heliosphere can be identified. Finite difference methods make it possible to obtain information for all particle energies in the entire heliosphere in one run. However, problems with a large spatial variation in coefficients require a very dense coordinate grid, i.e. large amounts of data to be stored, etc.

The long-term GCR variations can be calculated either by solving Equation (4), followed by averaging the solution over longitude, or by solving Equation (5). Nonetheless, in the latter case, we have to either neglect source term Q (6), which can often be unreasonable, or estimate Q without solving Equation (5). Note that earlier in [Kalinin, Krainev, 2014] we proposed an expression for Q for the simplest variant when the HMF polarity is the only longitude-dependent characteristic. Kalinin et al. [2021] have tested this expression by solving a 3D problem and have shown that it is insufficient, yet at the same time they have demonstrated (at least for particles with T=1 GeV) that the source term is smaller than the drift term in (5).

Thus, the main heliospheric factors important for the formation of recurrent GCR intensity variations include the main characteristics depending on all the three spatial coordinates: SW velocity, regular HMF and spectrum of its fluctuations, which determines the diffusion tensor, as well as the characteristics derived from the main ones — particle magnetic drift velocity

$$\mathbf{V}_D = \frac{pv}{3q} \left[\nabla \times \frac{\mathbf{B}}{B^2} \right], \qquad (7)$$

where v and q are the particle velocity and charge respectively; $\mathbf{B}$ is the regular HMF vector. To describe the long-term GCR intensity variations in 2D geometry, we have to know the longitude-averaged coefficients of Equation (4), as well as to estimate source term (6).

5. METHODS OF SIMULATING LONG-TERM GCR INTENSITY VARIATIONS WITH RESPECT TO CIRs

The CIR effect on the heliospheric characteristics important for GCR propagation is evidenced both by measurement data and by MHD calculations. The heliosphere structure (the latitudinal zone with waved HCS), which gives rise to CIRs, exists almost constantly (except for short periods of HMF inversion, when global HCS is violated, i.e. it does not continuously connect all longitudes [Krainev, 2019]). That is why, the corotating interaction regions and the HMF rarefaction regions surrounding them should be included in the models used to describe not only recurrent, but also long-term GCR intensity variations, and preferably explicitly.

Left panels in Figure 7 display the longitude dependence of V_r, B obtained from the MHD simulation and the 600 MeV proton intensity J calculated by the Monte Carlo method on a sphere r=0.94 AU along the equator. In the first approximation, we can see that the GCR intensity peaks coincide with the depressions in the longitude dependence of V_r and B, as well as the intensity depressions coincide with the SW velocity peaks. The longitude profiles of V_r, B, and J are compared in more detail in [Luo et al., 2020]. Comparing the results of intensity calculations with PAMELA spacecraft observations [Modzelewska et al., 2020] reveals two features: 1) the average level of the observed intensity is slightly higher than the calculated

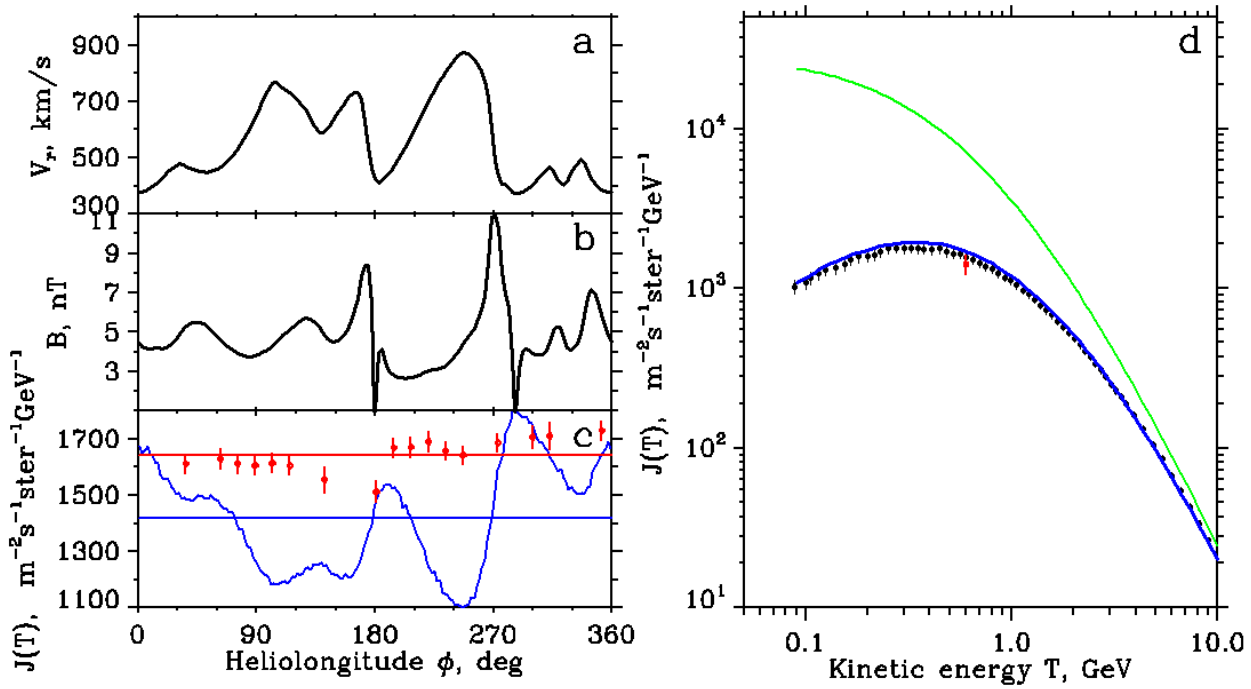

Figure 7. Longitude dependence of calculated heliospheric characteristics and GCR intensity and calculated energetic proton spectrum for CR 2066. On the left are the results of the calculation of heliospheric characteristics and GCR intensity on the sphere r=0.94 AU: panels *a*, *b* show the radial SW velocity component and the HMF strength along the equator respectively. Panel *c* is the GCR intensity with an energy of 600 MeV. The blue line is the values calculated in [Luo et al., 2020]; red diamonds with errors are the daily average values of this intensity measured by the PAMELA spacecraft [Modzelewska et al., 2020]. Horizontal lines of the corresponding color are the intensity values averaged over longitude. Panel *d*: the blue line is the kinetic spectrum of protons for CR 2066, calculated in [Luo et al., 2020]. The green curve shows the unmodulated proton spectrum used in the calculation; black icons with a bar (measurement error) are the spectrum as observed by the PAMELA spacecraft [Adriani et al., 2013]. The red dot with a bar (due to the intensity variation with longitude) is the latitude-averaged calculated intensity of protons with T=600 MeV

one (horizontal dashed lines of the corresponding color) and 2) the observed intensity variation is more than three times lower than the calculated one. For example, in the longitude range 240°–280° the variation (amplitude) in the calculated intensity ≈50 % of the average per rotation, with a maximum amplitude in observations ≈12 % of the average intensity (in the longitude range 180°–200°).

It appears likely that the discrepancy between the observations and the calculations of the GCR intensity is to some extent due to both the different radial distance (for observations r=1 AU, for calculations r=0.94 AU) and the different projection on the sphere (along the Earth orbit for observations, along the equator for calculations).

The most direct way to simulate the long-term GCR intensity variation is to use the scheme adopted for simulating recurrent variations when 1) the heliospheric characteristics are calculated for the *i*th Carrington rotation (with the mean time t_i) in the MHD approximation; 2) the GCR intensity $J_i(r, \theta, \varphi, T)$ is determined by solving transport 3D equations with coefficients found from the results of this 3D MHD calculation. It is natural to determine the intensity characterizing the long-term GCR intensity variations by averaging $J_i(r, \theta, \varphi, T)$ over longitude, $J(r, \theta, T, t_i) = \langle J_i(r, \theta, \varphi, T) \rangle_\varphi$.

The proton energy spectrum for CR 2066, shown by the blue line in Figure 7, *d*, was obtained by the Monte Carlo method in [Luo et al., 2020] and lies approximately at the upper boundary of the spectrum as observed by the PAMELA spacecraft. Yet, for each energy, it was obtained not by averaging over the longitude of the intensity calculated along Earth's trajectory, but is equal to the intensity at longitude φ=0° at the equator. In this figure is also a longitude-averaged calculated intensity of protons with T=600 MeV (icon with a bar, determined by the intensity variation with longitude), whose longitude dependence is shown in panel *c*. It can be seen that, at least for protons with this energy, the longitude-averaged calculated intensity subject to errors is also consistent with observations.

Nowadays, the long-term GCR intensity variations are well described by 3D models developed at North-West University (NWU, Potchefstroom, South Africa, see, e.g., [Potgieter, Vos, 2017; Aslam et al., 2019; Ngobeni et al., 2020, 2022]). Nevertheless, the only longitude-dependent characteristic is considered the direction (sunward/antisunward) of regular HMF, and describing the proton spectrum in a period requires taking into account not only the changes in the observed factors — the HCS quasi-tilt α_{qt} on the source surface, HMF strength B near the Earth orbit, and the general HMF polarity A (the sign B_r in the northern unipolar "hemisphere" of the heliosphere) — but also a set of descriptive factors (free pa-

rameters). Thus, the NWU 3D models include CIR effects not explicitly, but through the selection of free factors. At the same time, the NWU packets allow us to numerically solve modulation equations with coefficients that fully depend on all the three coordinates, and they can be used to tackle the problems with CIR effects in an explicit form.

As for the description of the long-term GCR variations with emulation of CIR effects in 2D models, the first such attempt was made in the LPI model [Kalinin et al., 2015]. By the term emulation used in articles in English is meant reproduction of not all, but the main or important properties of a phenomenon during simulation. It has been observed [Svirzhevskaya et al., 2001] that some features (sharp jumps) characteristic of time changes in the HCS quasi-tilt α_{qt} are manifested in the GCR intensity at both HMF polarities. This fact led to the conclusion that the diffusion characteristics may depend on α_{qt} due to the presence of CIRs in the zone of the HMF sector structure. Svirzhevsky et al. [2015], when analyzing HMF inhomogeneities along the trajectory of the Ulysses spacecraft, have found a difference in the spectral index inside ($\gamma_{HMF}\approx1.2$) and outside ($\gamma_{HMF}\approx0.8$) the zone of the HMF sector structure (in accordance with the behavior of this characteristic demonstrated in the bottom panel of Figure 4, *d*). Finally, in the model [Kalinin et al., 2015], a different dependence of the diffusion coefficient on rigidity, ($K \sim R^{\gamma_R}$, $\gamma_R = 2-\gamma_{HMF}$) in the zone of the sector structure and outside it was used to emulate this CIR effect. The authors, however, ignored the significant radial dependence of CIR effects obtained from MHD simulation data (see below). In addition, in the model [Kalinin et al., 2015], when solving Equation (5), an estimate of the source term *Q* was used, which, as shown in [Kalinin et al., 2021], does not fit well enough the exact source term calculated by solving the 3D equation.

Since in the NWU or LPI models the diffusion coefficients are axisymmetric and their spatial distribution is determined by the longitude-averaged HMF strength, it is interesting to study the radial-latitudinal distribution of difference Δ_{Par}^{MHD} (3), introduced in the previous section, between the HMF strength, calculated in the MHD approximation, and the longitude-averaged Parker HMF strength without CIR effects.

Note the qualitative features of this distribution illustrated in Figure 8. In the radial direction, the MHD simulation domain is divided into a near-solar region ($r < 3$–5 AU), where the HMF strength is greater than that in the absence of CIR, and an outer region ($(3\div5)$ AU $< r \le r_{out}^{MHD} = 28.4$ AU) with a relative weakening of the field at low and high latitudes with some strengthening in narrow ranges of midlatitudes. The position of these latitudinal zones in the outer region in the first approximation is seen to correlate with the latitudinal HCS boundaries and is symmetrical about the magnetic equator at the base of the heliosphere. The radial distribution in this outer region indicates the possibility of extending the same ratio to the heliosphere external to the MHD simulation domain $r_{out}^{MHD} < r < r_{out}$.

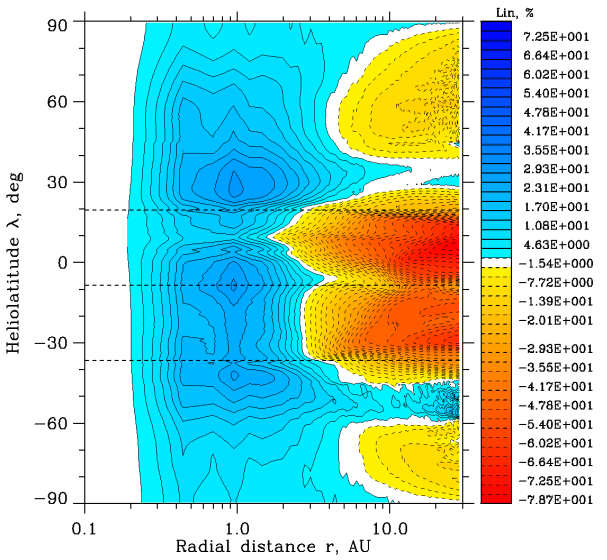

Figure 8. Radial-latitudinal distribution of longitude-averaged relative difference Δ_{Par}^{MHD} (3) between the HMF strength, calculated in the MHD approximation [Luo et al., 2020], and the Parker HMF assuming the absence of interaction between SW streams of different speed. Horizontal dashed lines are the latitudinal HCS boundaries and the magnetic equator at the base of the heliosphere

6. DISCUSSION AND CONCLUSIONS

It follows from the results of Section 2 that data from the spacecraft that scanned large areas of the heliosphere suggests (albeit indirectly) a strong CIR effect on the characteristics of both the SW velocity field and regular HMF and its fluctuations. It is important for simulation of GCR variations that due to the interaction between SW streams of different speed, the applicability of the frequently used Parker HMF model is questionable, at least in the zone of the HMF sector structure in the inner heliosphere (r<10 AU). Moreover, it is significant that the characteristics of the spectrum of HMF inhomogeneities, which determine the diffusion coefficients of cosmic rays, differ greatly in the zone of the sector structure and outside it and may change with distance.

The MHD calculation results given in Section 3 also indicate a significant change with distance in the distribution of the characteristics of both the SW velocity and HMF, including the shape of the heliospheric current sheet. An important consequence for simulating GCRs is the distribution of the absolute radial HMF component, which varies greatly with distance from the Sun. If this value is constant within 10 % near the Sun, by $r\approx10$ AU its spread relative to the mean is already ~70 % and then changes slightly to the outer boundary of MHD simulation. This fact casts doubt on the assumption, often applied to GCR simulation, that measuring the radial HMF component in the Earth orbit makes it possible to extend it to all latitudes; and using the Parker HMF model, to the entire heliosphere. These strong changes in the large-scale characteristics of the heliosphere, crucial for the long-term GCR variations, are associated with the formation and evolution of CIRs.

The idea emerges that the best approach to simulating the longitude-averaged GCR intensity in order to describe its long-term variations, which explicitly considers CIRs effects, is the most direct — to use the scheme adopted for simulating recurrent variations, and then to average the calculation results over longitude. Moreover, it would be very desirable to supplement the 3D Monte Carlo intensity calculations with finite difference calculations, although this is a rather difficult task.

As for the possibility of describing the long-term GCR variations with emulation of CIR effects in 2D models, or even in 3D models with longitude-independent SW velocity and diffusion coefficients, this is still an open question. Doubts also arise over the possibility of using as observable parameters the quasi-tilt model of HCS calculated on the source surface near the Sun and the heliospheric characteristics, averaged over the solar rotation, measured in the vicinity of the Earth orbit, specifically the absolute radial HMF component. To emulate CIR effects, much more meaningful input parameters should be used.

Some interesting conclusions can be drawn from the radial-latitudinal distribution of the longitude-averaged relative difference between the HMF strength, calculated in the MHD approximation, and that estimated without considering the interaction between SW streams of different speed. As follows from the MHD simulation results, in the near-solar region ($r < (3 \div 5)$ AU) the interaction between SW streams of different speed leads, on average, to HMF enhancement at all latitudes. In the outer region ($(3 \div 5)\ \text{AU} < r \le r_{\text{out}}^{\text{MHD}}$), the HMF strength due to this interaction weakens on average at low and high latitudes with some strengthening in narrow ranges of midlatitudes.

If this effect — the weakening of the HMF strength in the middle heliosphere — is extended to the region external to the MHD simulation domain ($r_{\text{out}}^{\text{MHD}} < r < r_{\text{out}}$), it can be cautiously concluded that in many regions of such a heliosphere, modified by the interaction between SW streams of different velocity, the modulated GCR intensity may be higher than that without this modification. Note that this paradoxical conclusion fits well with the calculation results [Kopp et al., 2017; Guo, Florinski, 2014], although these authors use heliospheric models to calculate the GCR intensity, without taking into account the CIR effect, which are very different from the model we apply. Thus, we attribute the effect of GCR modulation weakening with respect to CIRs, perhaps the most significant for long-term intensity variations, to a weakening of the HMF strength in the middle heliosphere due to the evolution of rarefied areas of CIRs.

However, as can be seen from comparing the calculation results with observations, before making confident quantitative conclusions about the effect of the interaction between solar wind streams of different speed on heliospheric characteristics and GCR intensity, it is necessary to refine the procedures of both MHD simulation of heliospheric factors and GCR intensity calculations by the Monte Carlo method. Note also that in this paper we make use of the MHD simulation and MC calculation results on a rather rare sample from the original mesh on which the simulation was carried out. To make the results clearer (for example, to construct HMF lines, the position of the contact surface and shock waves, to build trajectories of GCR pseudoparticles), we should employ the entire initial mesh. Besides, some conclusions drawn from the simulation of heliospheric characteristics and GCR intensity may be specific to the Carrington rotation considered. To draw more reasonable conclusions, it is necessary to examine the situation in other periods. It is also useful to analyze the results of simplified MHD simulations with simple boundary conditions: the simplest shape of HCS, a given dependence of SW velocity on angular distance from HCS, etc.

Finally, in order to understand the laws of formation and evolution of the corotating interaction regions of the solar wind and its related GCR intensity variations in the heliosphere in the solar cycle, it is necessary to figure out how these phenomena are related to the development of both branches (poloidal and toroidal) of solar magnetic fields.

We are grateful to all the teams of researchers who present their results on the Internet. Xi Luo acknowledges the support from the Taishan Scholar Project of Shandong Province (202103143) and the grant from the National Science Foundation of China (NSFC, U2106201).

REFERENCES

Adriani O., Barbarino G.C., Bazilevskaya G.A., Bellotti R., Boezio M., Bogomolov E.A., et al. Time dependence of the proton flux measured by PAMELA during the 2006 July – 2009 December solar minimum. *Astrophys. J.* 2013, vol. 765:91, no. 2. DOI: 10.1088/0004-637X/765/2/91.

Aslam O.P.M., Bisschoff D., Potgieter M.S., Boezio M., Munini R. Modeling of heliospheric modulation of cosmic-ray positrons in a very quiet heliosphere. *Astrophys. J.* 2019, vol. 8736: 70, no. 1. DOI: 10.3847/1538-4357/ab05e6.

Belcher J.W., Davis L. Large-amplitude Alfvén waves in the interplanetary medium, 2. *J. Geophys. Res.* 1971, vol. 76, iss. 16, p. 3534. DOI: 10.1029/JA076i016p03534.

Burlaga L.F., Ness N.F., Wang J.-M., Sheeley N.R. Heliospheric magnetic field strength and polarity from 1 to 81 AU during the ascending phase of solar cycle 23. *J. Geophys. Res.* 2002, vol. 107, no. A11, p. 1410. DOI: 10.1029/2001JA009217.

Gosling J.T., Pizzo V. Formation and evolution of corotating interaction regions and their three dimensional structure. *Space Sci. Rev.* 1999, vol. 89, pp. 21–52. DOI: 10.1023/A:1005291711900.

Guo X., Florinski V. Corotating interaction regions and the 27 day variation of galactic cosmic rays intensity at 1 AU during the cycle 23/24 solar minimum. *J. Geophys. Res.: Space Phys.* 2014, vol. 119, iss. 14, pp. 2411–2429. DOI: 10.1002/2013JA019546.

Guo X., Florinski V. Galactic cosmic-ray intensity modulation by corotating interaction region stream interfaces at 1 AU, *Astrophys. J.* 2016, vol. 826:65, no. 1. DOI: 10.3847/0004-637X/826/1/65.

Hundhausen A.J. Coronal Expansion and Solar Wind, *Springer-Verlag Berlin Heidelberg New York*. 1972, 238 p. DOI: 10.1007/978-3-642-65414-5.

Jokipii J.R., Levy E.H., Hubbard W.B. Effects of particle drift on cosmic-ray transport. I. General properties, application to solar modulation. *Astrophys. J.* 1977, vol. 213, p. 861. DOI: 10.1086/155218.

Kalinin M.S., Krainev M.B. Two dimensional transport equation for galactic cosmic rays as a consequence of a reduction of the three-dimensional equation. *Geomagnetizm and Aeronomy*. 2014, vol. 54, no. 4, pp. 423–429. DOI: 10.7868/S0016794014040051.

Kalinin M.S., Bazilevskaya G.A., Krainev M.B., Svirzhevsky N.S., Svirzhevskaya A.K., Stozhkov Yu.I. Description of galactic cosmic ray intensity in the last three solar activity minima. *Bull. Russ. Acad. Sci. Phys.* 2015, vol. 79, no. 5, pp. 606–608. DOI: 10.3103/S1062873815050238.

Kalinin M.S., Krainev M.B., Gvozdevsky B.B., Aslam O.P.M., Ngobeni M.D., Potgieter M.S. On the transition from 3D to 2D transport equations for a study of long-term cosmic-ray intensity variations in the heliosphere. 2021. POS(ICRC2021)1323. https://pos.sissa.it.

Khabarova O., Obridko V. Puzzles of the interplanetary magnetic field in the inner heliosphere. *Astrophys. J*. 2012, vol. 761: 82. DOI: 10.1088/0004-637X/761/2/82.

Kopp A., Wiengarten T., Fichtner H., Effenberger F., Kühl P., Heber B., Raath J.-L., Potgieter M. Cosmic-ray transport in heliospheric magnetic structures. II. Modeling particle transport through corotating interaction regions. *Astrophys. J*. 2017, vol. 837:37, no. 1. DOI: 10.3847/1538-4357/aa603b.

Kóta J., Jokipii J.R. Effects of drift on the transport of cosmic rays. VI. A three-dimensional model including diffusion. *Astrophys. J*. 1983, vol. 265, pp. 573–581. DOI: 10.1086/160701.

Kóta J., Jokipii J.R. The role of corotating interaction regions in cosmic-ray modulation, *Geophys. Res. Lett.* 1991, vol. 18, iss. 10, pp. 1797–1800. DOI: 10.1029/91GL02307.

Kóta J, Jokipii J.R. Modeling of 3-D corotating cosmic-ray structures in the heliosphere, *Space Sci. Rev*. 1998, vol. 83, pp. 137–145. DOI: 10.1007/978-94-017-1189-0_12.

Krainev M.B. Manifestations of two branches of solar activity in the heliosphere and GCR intensity. *Solar-Terr. Phys.* 2019, vol. 5, iss. 4, pp. 10–20. DOI: 10.12737/stp-54201902.

Krainev M.B., Bazilevskaya G.A., Borkut I.K., Mayorov A.K. Relationship between the longitude distribution of the heliospheric characteristics and the GCR intensity in 2007–2008 and 2014–2015. *Physics of Atomic Nuclei*. 2018, vol. 81, iss. 9, pp. 1355–1361. DOI: 10.1134/S1063778818090156.

Krymskiy G.F. Diffusion mechanism of diurnal cosmic-ray variation, *Geomagnetizm end Aeronomy*. 1964, vol. 4, pp. 763–769.

Luo X., Zhang M., Feng X., Potgieter M, Shen F., Bazilevskaya G.A. A numerical study of the effects of corotating interaction regions on cosmic-ray transport, *Astrophys. J*. 2020, vol. 899:90, no. 2. DOI: 10.3847/1538-4357/aba7b5.

Mays M.L., Taktakishvili A., Pulkkinen A., Macneice P.J. Ensemble modeling of CMEs using the WSA-ENLIL+Cone model. *Solar Phys.* 2015, vol. 290, iss. 6, pp. 1775–1814. DOI: 10.1007/s11207-015-0692-1.

Modzelewska R., Alania M.V. Dependence of the 27-day variation of cosmic rays on the global magnetic field of the Sun, *Adv. Space Res*. 2012, vol. 50, iss. 6, pp. 716–724. DOI: 10.1016/j.asr.2011.07.022.

Modzelewska R., Bazilevskaya G.A., Boezio M., Koldashov S.V., Krainev M.B., Marcelli N., Mayorov A.G., Mayorova M.A., Munini R., Troitskaya I. K., Yulbarisov R.F., Luo X., Potgieter M.S., Aslam O.P.M. Study of the 27 day variations in GCR fluxes during 2007–2008 based on PAMELA and ARINA observations. *Astrophys. J*. 2020, vol. 904:3, p. 13. DOI: 10.3847/1538-4357/abbdac.

Ngobeni M.D., Aslam O.P.M., Bisschoff D., Potgieter M.S., Ndiitwani D.C., Boezio M., Marcelli N., Munini R., Mikhailov V.V., Koldobskiy S.A. The 3D numerical modeling of the solar modulation of galactic protons and helium nuclei related to observations by PAMELA between 2006 and 2009. *Astrophys. Space Sci.* 2020, vol. 365:182. DOI: 10.1007/s10509-020-03896-1.

Ngobeni M.D., Potgieter M.S., Aslam O.P.M., Bisschoff D., Ramokgaba I.I., Ndiitwani D.C. Simulations of the solar modulation of helium isotopes constrained by observations, *Adv. Space Res.* 2022, vol. 69, iss. 5, pp. 2330–2341. DOI: 10.1016/j.asr.2021.12.018.

Odstrcil D. Modeling 3-D solar wind structure *Adv. Space Res.* 2003, vol. 32, iss. 4, pp. 49–506. DOI: 10.1016/S0273-1177(03)00332-6.

Parker E.N. Dynamics of the interplanetary gas and magnetic fields. *Astrophys. J*. 1958a, vol. 128, p. 664. DOI: 10.1086/146579.

Parker E.N. Cosmic ray modulation by solar wind. *Phys. Rev*. 1958b, vol. 110, iss. 6, p. 1445. DOI: 10.1103/PhysRev.110.1445.

Parker E.N. The passage of energetic charged particles through interplanetary space, *Planet. Space Sci*. 1965, vol. 13, iss. 1, pp. 9–49. DOI: 10.1016/0032-0633(65)90131-5.

Pizzo V.J., Gosling J.T. 3-D simulation of high-latitude interaction regions: comparison with Ulysses results. *Geophys. Res. Lett.* 1994, vol. 21, iss. 18, pp. 2063–2066. DOI: 10.1029/94GL01581.

Potgieter M.S., Vos E.E. Difference in the heliospheric modulation of cosmic-ray protons and electrons during the solar minimum period of 2006 to 2009. *Astronomy and Astrophysics*. 2017, vol. 601, no. 23. DOI: 10.1051/0004-6361/201629995.

Richardson I.G. Solar wind stream interaction regions throughout the heliosphere. *Living Reviews Solar Physics*. 2018, vol. 15, no. 1, pp. 1–95. DOI: 10.1007/s41116-017-0011-z.

Riley P., Linker J.A., Lionello R., Mikic Z. Corotating interaction regions during the recent solar minimum: The power and limitations of global MHD modeling. *J. Atmos. Solar-Terr. Phys.* 2012, vol. 83, pp. 1–10. DOI: 10.1016/j.jastp.2011.12.013.

Shen F., Yang Z., Zhang J., Wei W., Feng X. Three-dimensional MHD simulation of solar wind using a new boundary treatment: comparison with in situ data at Earth, *Astrophys. J*. 2018, vol. 866:18, no. 1. DOI: 10.3847/1538-4357/aad806.

Schulz M. Interplanetary sector structure and the heliomagnetic equator, *Astrophys. Space Sci*. 1973, vol. 24, pp. 371–384. DOI: 10.1007/BF02637162.

Simpson J.A. A brief history of recurrent solar modulation of the galactic cosmic rays (1937–1990). *Space Sci. Rev*. 1998, vol. 83, pp. 169–176. DOI: 10.1007/978-94-017-1189-0_15.

Smith E.J. Solar cycle evolution of the heliospheric magnetic field: The Ulysses legacy. *J. Atmos. Solar-Terr. Phys.* 2011, vol. 73, iss. 2-3, pp. 277–289. DOI: 10.1016/j.jastp.2010.03.019.

Svirzhevsky N.S., Bazilevskaya G.A., Kalinin M.S., Krainev M.B., Svirzhevskaya A.K., Stozhkov Yu.I. Galactic cosmic ray intensity simulation with spatial and temporal dependence of fluctuations of the helioshperic magnetic field. *Bull. Russ. Acad. Sci. Phys*. 2015, vol. 79, no. 5, pp. 609–612. DOI: 10.3103/S1062873815050391.

Svirzhevsky N.S., Bazilevskaya G.A., Kalinin M.S., Krainev M.B., Makhmutov V.S., Svirzhevskaya A.K., Stozhkov Yu.I. Heliospheric magnetic field and the Parker model. *Geomagnetizm end Aeronomiya*. 2021, vol. 61, no. 3, pp. 299–311. DOI: 10.1134/S0016793221030154.

Svirzhevskaya A.K., Svirzhevsky N.S., Stozhkov Yu.I. Step-like variations of cosmic rays and their relation to an inclination of the heliospheric current sheet. *Proceedings of ICRC* 2001, pp. 3843–3846.

Wang Y.-M., Sheeley N.R. Solar wind speed and coronal flux-tube expansion. *Astrophys. J.* 1990, vol. 355, pp. 726–732, DOI: 10.1086/168805.

Wiengarten T., Kleimann J., Fichtner H., Kühl P., Kopp A., Heber B., Kissmann R. Cosmic ray transport in heliospheric magnetic structures. I. Modeling background solar wind using the CRONOS magnetohydrodynamic code. *Astrophys. J.* 2014, vol. 788, no. 1, p. 80. DOI: 10.1088/0004-637X/788/1/80.

Yanenko N.N. Metod drobnykh shagov resheniya mnogomernykh zadach matematicheskoy fiziki, Novosibirsk, Nauka Publ. 1967. 197 p. [The method of fractional steps for solving multidimensional problems of mathematical physics. Berlin. Springer Publ. 1971. 156 p.]

Zhang M.A path integral approach to the theory of heliospheric cosmic-ray modulation. *Astrophys. J.* 1999a, vol. 510, no. 2, pp. 715–725. DOI: 10.1086/306624.

Zhang M.A Markov stochastic process theory of cosmic-ray modulation, *Astrophys. J.* 1999b, vol. 513, pp. 409–420. DOI: 10.1086/306857.

URL: http://wso.stanford.edu (accessed January 30, 2023).

URL: http://cr0.izmiran.ru/mosc/main.htm (accessed January 30, 2023).

URL: http://omniweb.gsfc.nasa.gov/ (accessed January 30, 2023).

Original Russian version: Krainev M.B., Kalinin M.S., Bazilevskaya G.A., Svirzhevskaya A.K., Svirzhevsky N.S., Xi Luo, Aslam O.P.M., Fang Shen, Ngobeni M.D., Potgieter M.S., published in Solnechno-zemnaya fizika. 2023. Vol. 9. Iss. 1. P. 10–21. DOI: 10.12737/szf-91202302.

How to cite this article

Krainev M.B., Kalinin M.S., Bazilevskaya G.A., Svirzhevskaya A.K., Svirzhevsky N.S., Xi Luo, Aslam O.P.M., Fang Shen, Ngobeni M.D., Potgieter M.S. Manifestation of solar wind corotating interaction regions in GCR intensity variations. *Solar-Terrestrial Physics*. 2023. Vol. 9. Iss. 1. P. 9–20. DOI: 10.12737/stp-91202302.